An Advanced Frequency-based Energy Management of Hybrid Energy Storage Systems for Microgrids

Mario Porru, Alessandro Serpi, Andrea Salimbeni, Alfonso Damiano
Department of Electrical and Electronic Engineering
University of Cagliari
Cagliari, Italy
mario.porru@diee.unica.it

***Abstract*—An advanced Frequency-Based energy Management (FBM) suitable for Hybrid Energy Storage Systems (HESSs) in Microgrids (MGs) is presented in this paper. The HESS is made up of Batteries (B) and Supercapacitors (S) and it has to provide both peak shaving and power quality. A frequency-based power split criterion is introduced, namely the B power profile is synthesized through an appropriate low-pass filter, while S has to cope with sudden and fast power fluctuations. In addition, in order to enable a suitable peak shaving capability, an appropriate management algorithm is developed based on the forecasted MG power profile. As a result, suitable B power thresholds can be defined in accordance with both B power and energy constraints over a given time horizon. This can be adapted also in real-time in order to benefit from more accurate forecasting and B energy status. The effectiveness of the proposed FBM is proved by numerical simulations, which refer to the MG of the German island of Borkum.**

Keywords*— *Batteries, Energy Management, Energy Storage, Microgrids, Supercapacitors.

I. Introduction

Hybrid Energy Storage Systems (HESSs) represent a very promising solution for increasing Microgrid (MG) performances in the next future [1], [2]. This is because the issues arising from the use of only one energy storage system can be overcome by employing two or more complementary energy storage technologies jointly. In this regard, the combination of Batteries (B) and Supercapacitors (S) has shown superior performances compared to other hybrid solutions, from both technical and economic points of view [3]–[5]. Particularly, B are more suited than S for providing energy services [6], [7], such as load levelling and peak shaving, due to higher energy density. Whereas S are characterized by much higher power density compared to B [8], [9], revealing them as a suitable choice for providing power services (power quality, short-term forecasting error compensation, etc.). Consequently, the power split criterion is fundamental in order to exploit the HESS to the maximum extent.

Several strategies for HESS energy management in MGs have been proposed in the literature [10]–[17]. The most popular approach consists of identifying low-frequency and high-frequency harmonic contents of the overall HESS power profile by means of low/high pass filters [10]–[12]. The low-frequency HESS power profile has to be tracked by B, which does not compensate for high-frequency power fluctuations in order to preserve its performances and life cycle. High-frequency HESS power profile can thus be handled by S, also because it is generally characterized by a relatively poor energy content. However, frequency-based management approaches are not able to account for B energy constraints properly, thus they are generally combined with rule-based and/or fuzzy logic algorithms in order to take into account HESS operating constraints [13]–[15].

In this context, a novel Frequency-Based energy Management approach (FBM) suitable for HESS to be installed in MGs is presented in this paper. It is developed with the aim of enabling the HESS to provide both energy and power services, namely peak shaving and power quality. Adequate peak shaving capability is achieved by B through a management algorithm; this identifies suitable power thresholds based on forecasted MG power profile over a given time horizon in order to guarantee the compliance with both B energy and power constraints. In addition, the frequency-based power split criterion prevents B from coping with sudden power fluctuations, which are handled by S successfully due to their poor energy content. The proposed FBM is validated through numerical simulations, which have been performed referring to MG data measured in the German island of Borkum.

II. MG and HESS Modeling

A. Microgrid

An MG is generally made up of several distributed generators and loads, clustered as shown in Fig. 1. It is thus

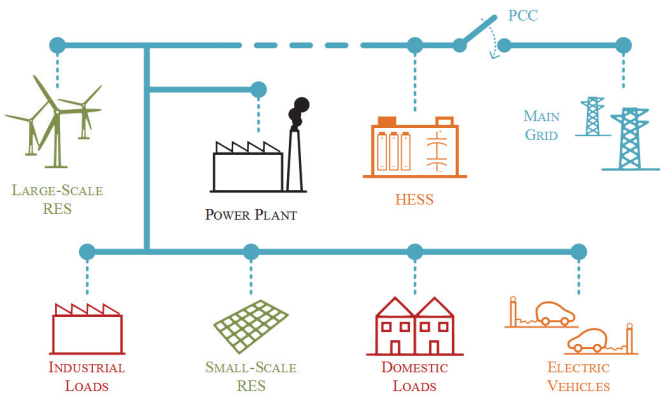

Fig. 1. Schematic representation of an MG.

This work is developed within the project NETfficient, "Energy and Economic Efficiency for Today's Smart Communities through Integrated Multi Storage Technologies". This project has received funding from the European Union's Horizon 2020 research and innovation programme under grant agreement No 646463.

 Published paper's DOI: 10.1109/IECON.2017.8217335

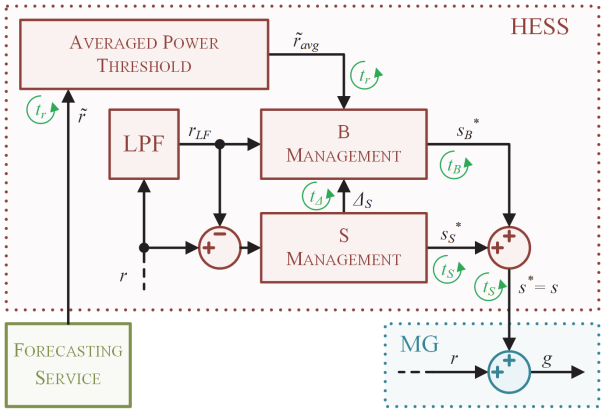

Fig. 2. Overall block control scheme of the proposed FBM, in which LPF denotes the low-pass filter.

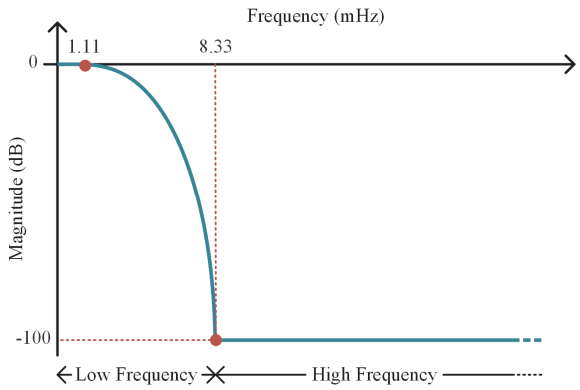

Fig. 3. The transfer function of the LPF employed for the FBM.

possible to define its residual power at the Point of Common Coupling (PCC) as

$$r = \sum_i p_i + \sum_j l_j \tag{1}$$

in which p_i and l_j denote the power delivered by the i-th generator and drawn by the j-th load respectively. Particularly, p_i is always positive, whereas l_j is always negative. Consequently, an MG acts as either a load or a generator depending on the sign of r. Assuming the HESS coupled with the PCC directly, the power balance at that node can be easily expressed as

$$g = r + s \tag{2}$$

where s and g denotes the overall power exchanged by the MG with the HESS and the main grid respectively. A positive s value thus means that HESS is discharging, the opposite occurring over an HESS charging process.

B. Hybrid Energy Storage System

The HESS considered in this paper is made up of two energy storage units, namely Batteries (B) and Supercapacitors (S). Consequently, HESS overall power is made up of two contributions as

$$s = s_B + s_S \tag{3}$$

where s_B and s_S denote the power exchanged by B and S respectively. Similarly, the overall energy stored in the HESS can be expressed as

$$e = e_B + e_S \tag{4}$$

in which e_B and e_S vary in accordance with s_B and s_S respectively. Denoting by η_c and η_d the charging and discharging efficiency, the energy time variation of both B and S can be defined as

$$\frac{de_X}{dt} = -\left(\frac{1}{\eta_{d,X}} \frac{s_X + |s_X|}{2} + \eta_{c,X} \frac{s_X - |s_X|}{2} \right), \quad X \in \{B,S\}. \tag{5}$$

Furthermore, power and energy of both B and S are bounded in accordance with appropriate constraints as

$$s_{X,min} \le s_X \le s_{X,max}, \quad X \in \{B,S\} \tag{6}$$

$$e_{X,min} \le e_X \le e_{X,max}, \quad X \in \{B,S\} \tag{7}$$

in which upper and lower limits depend on the specific energy storage technology, size and operating conditions. In this regard, it is worth noting that S power constraint is much more relevant than S energy constraint as far as S is employed for MG power services. This is because residual power fluctuations are generally characterized by a high-frequency and poor energy content. Different considerations should be made for B energy and power constraints, which are both of paramount importance in order to provide energy services appropriately. Consequently, an appropriate B energy and power management cannot be achieved by means of a frequency-based power split criterion only, but it requires a more advanced solution, as detailed in the following section.

III. Frequency-Based HESS Energy Management

The overall block control scheme of the proposed FBM is depicted in Fig. 2. It can be seen that the low-frequency content of the MG residual power profile (r_{LF}) is determined in real-time by an appropriate digital low-pass filter, whose transfer function is depicted in Fig. 3. This does not account for magnitude ripple, while the transition band has been chosen between 1.11 mHz and 8.33 mHz.

Since r_{LF} is generally characterized by a significant energy content, B could hardly compensate for such a large MG residual power profile due to both power and energy constraints. Particularly, as far as peak shaving is concerned, r_{LF} should be deprived of its average power component over a given time horizon T, thus reducing the r_{LF} energy content significantly. This average power component ($\tilde{r}_{avg}$) could be computed based on forecasted MG residual power profile. Consequently, by taking into account B charging and discharging efficiencies in providing full peak-shaving, $\tilde{r}_{avg}$ can be computed by solving the following equation:

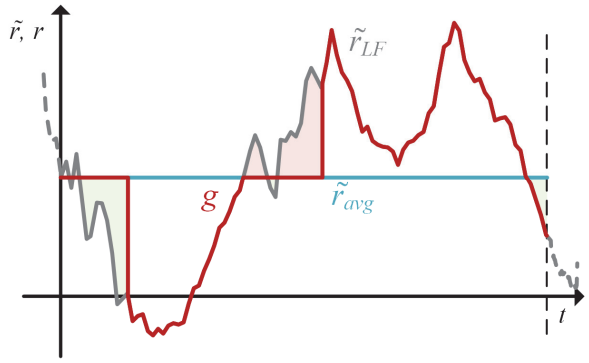

Fig. 4. An example of MG residual power profile, together with the B power profile synthesized in accordance with (10).

$$\int_{t}^{t+T}\left(\alpha_B\left(\tilde{r}_{avg}-\tilde{r}\right)+\beta_B\left|\tilde{r}_{avg}-\tilde{r}\right|\right)dt=0 \tag{8}$$

where α_B and β_B depend on B charging and discharging efficiencies as

$$\alpha_B=\frac{1}{2}\left(\frac{1}{\eta_{d,B}}+\eta_{c,B}\right),\quad \beta_B=\frac{1}{2}\left(\frac{1}{\eta_{d,B}}-\eta_{c,B}\right). \tag{9}$$

The B power profile could be thus determined in real-time in accordance with B power and energy constraints as

$$s_B=\left(-r_{LF}+\tilde{r}_{avg}\right)\Big\rangle_{s_{B,min}}^{s_{B,max}} \tag{10}$$

in which the operator $\rangle$ limits s_B between $s_{B,min}$ and $s_{B,max}$, thus complying with (7). In addition, $\tilde{r}_{avg}$ can be updated at a suitable time rate in order to benefit from more accurate forecasting and B energy status.

However, employing (10) does not generally lead to adequate peak shaving capability unless large B capacity is employed. This is because B is rapidly filled in as soon as r_{LF} overcomes $\tilde{r}_{avg}$. The opposite occurs when r_{LF} drops below $\tilde{r}_{avg}$, namely B is quickly discharged to its minimum energy level. Consequently, B acts for short time periods only, which do not generally correspond to r_{LF} peak values, as highlighted in Fig. 4. Hence, in order to avoid poor peak shaving capability, two additional power thresholds can be defined based on the B energy constraint, as shown in Fig. 5. Particularly, positive and negative power thresholds ($\tilde{r}^+$ and $\tilde{r}^-$) can be determined by the iterative procedure summarized in Fig. 6. Starting from $\tilde{r}^+ = \tilde{r}^- = \tilde{r}_{avg}$, the B power profile provided by (10) is considered at first, together with the corresponding B energy evolution. Since this does not generally comply with (7), if the first violation implies overcoming $e_{B,max}$, $\tilde{r}^+$ is increased in order to reduce the energy drawn by B in accordance with the following equation:

$$s_B=\left(-r_{LF}+\tilde{r}^+\right)\Big\rangle_{s_{B,min}}^{0}+\left(-r_{LF}+\tilde{r}^-\right)\Big\rangle_{0}^{s_{B,max}}. \tag{11}$$

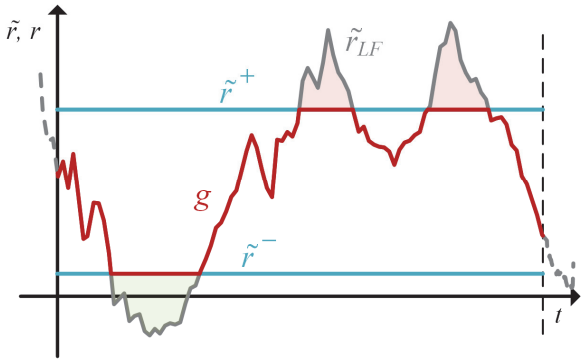

Fig. 5. An example of MG residual power profile, together with the B power profile synthesized in accordance with (11).

Therefore, e_B is computed again in accordance with (11) and (5), then a new iteration starts: if another violation is detected, $\tilde{r}^+$ is increased or $\tilde{r}^-$ is decreased in order to reduce the energy exchanged by B with the MG appropriately. The proposed procedure ends when the s_B profiles given by (11) leads to an e_B profile that complies with (7), meaning that the optimal pair of thresholds have been achieved.

In conclusion, the S power profile is computed directly in real-time in accordance with the high-frequency content of the residual power profile (r–r_{LF}), as already shown in Fig. 2. Particularly, s_S can be determined as

$$s_S=\left(-r+r_{LF}\right)\Big\rangle_{s_{S,min}}^{s_{S,max}}. \tag{12}$$

It is worth noting that (12) generally complies with (7) since a poor energy content of the high-frequency MG residual power profile is foreseen. Consequently, there is no need of advanced energy constraint management, as required by B. However, an appropriate average power (Δ_S) is considered in order to hold the S energy level around a given intermediate value, as pointed out in Fig. 2. The HESS power profiles can be thus computed as summarized in TABLE I.

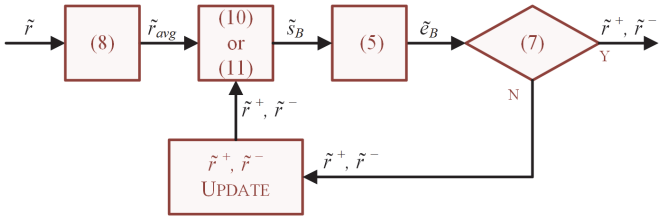

Fig. 6. Flowchart of the proposed FBM energy management strategy.

TABLE I FREQUENCY-BASED HESS MANAGEMENT (FBM)

	$e_B = e_{B,max}$	$e_{B,min} < e_B < e_{B,max}$	$e_B = e_{B,min}$
s_B^*	0	$\left(-r_{LF}+\tilde{r}^+\right)\Big\rangle_{s_{B,min}}^{0}+\left(-r_{LF}+\tilde{r}^-\right)\Big\rangle_{0}^{s_{B,max}}$	0
	$e_S = e_{S,max}$	$e_{S,min} < e_S < e_{S,max}$	$e_S = e_{S,min}$
s_S^*	0	$\left(-r+r_{LF}\right)\Big\rangle_{s_{S,min}}^{s_{S,max}}$	0

IV. SIMULATIONS

The proposed FBM has been validated by means of a simulation study, which is carried out in the Matlab environment by referring to the MG of Borkum. It is a German island located in the North Sea (30.7 km^2, 5181 inhabitants) and it is characterized by both conventional and RES power plants, i.e. CHP, wind and photovoltaic, as highlighted in TABLE II. In addition, the PCC consists of four submarine cables that enable a bidirectional power flow with the mainland. The HESS consists of an active configuration that allows B and S to be managed independently. Particularly, B consists of Lithium Iron Phosphate batteries ($LiFePO_4$) which are coupled to the DC-link of the grid-tie inverter directly. Whereas S is coupled to the DC-link through a DC-DC converter. Both B and S main specifications are resumed in TABLE III.

Two different FBMs have been considered for simulations: the first case (FBM-A) refers to the employment of a single power threshold ($\tilde{r}_{avg}$), while the two different power thresholds proposed in this paper ($\tilde{r}^+$ and $\tilde{r}^-$) have been employed in the second case (FBM-B). The refresh time-rate has been set to 15 min in both cases, while the time horizon has been varied from 24 h to 6 h.

TABLE II BORKUM POWER PLANTS

	Power Plant	*Installed Power [kW]*
Medium Voltage	Wind	3600
	Photovoltaic	1387
	Total	4987
Low Voltage	Photovoltaic	953
	CHP	891
	Total	1844
Total	Total	6831

TABLE III HESS PARAMETERS AND RATED VALUES

	Parameter	*Value*	*Unit*
B	Rated Charging Power	250	kW
	Rated Discharging Power	500	kW
	Total (Usable) Energy	500 (400)	kWh
	Max (min) Stored Energy	450 (50)	kWh
	Round-Trip Efficiency	92	%
S	Rated Power	1108	kW
	Total (Usable) Energy	9 (6)	kWh
	Max (min) Stored Energy	11.4 (2.4)	kWh
	Round-Trip Efficiency	90	%

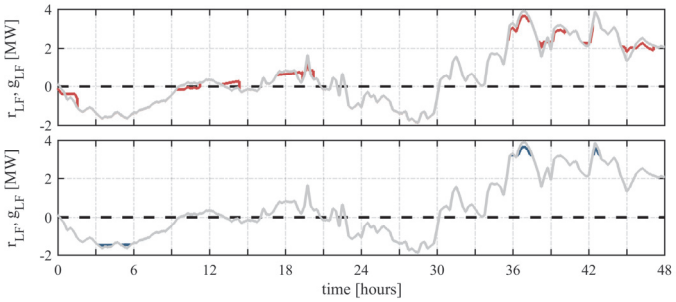

Fig. 7. The r_{LF} (gray) and g_{LF} profiles by FBM-A (top, red) and FBM-B (bottom, blue) at $T = 24$ h.

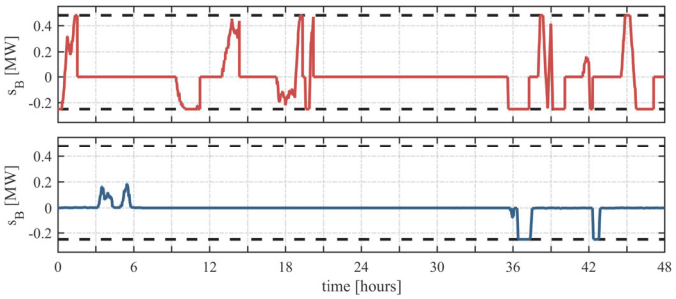

Fig. 8. B power evolutions by FBM-A (top) and FBM-B (bottom) at $T = 24$ h.

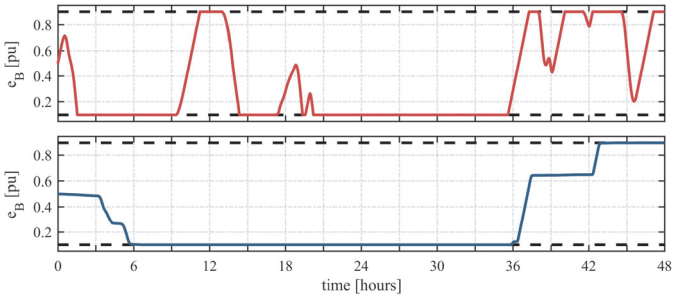

Fig. 9. B energy level by FBM-A (top) and FBM-B (bottom) at $T = 24$ h.

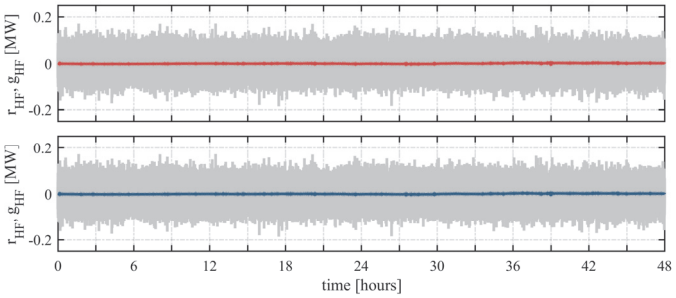

Fig. 10. The r_{HF} (gray) and g_{HF} profiles by FBM-A (top, red) and FBM-B (bottom, blue) at $T = 24$ h.

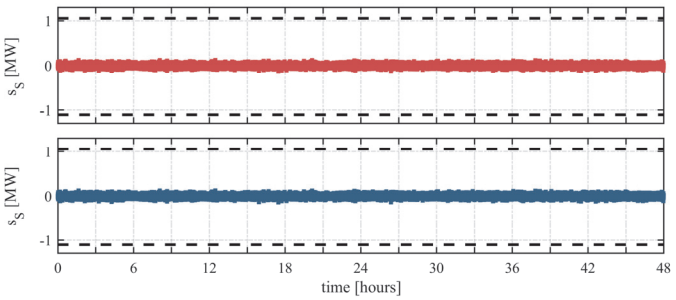

Fig. 11. S power evolution by FBM-A (top) and FBM-B (bottom) at $T = 24$ h.

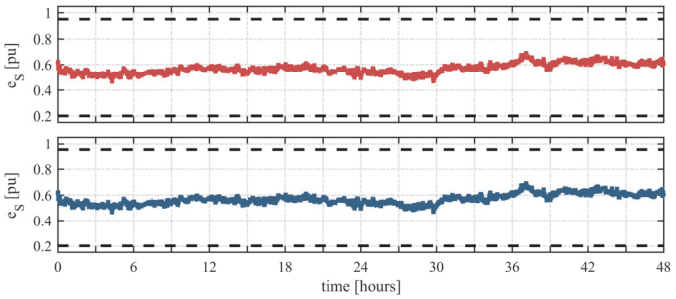

Fig. 12. S energy level by FBM-A (top) and FBM-B (bottom) at $T = 24$ h.

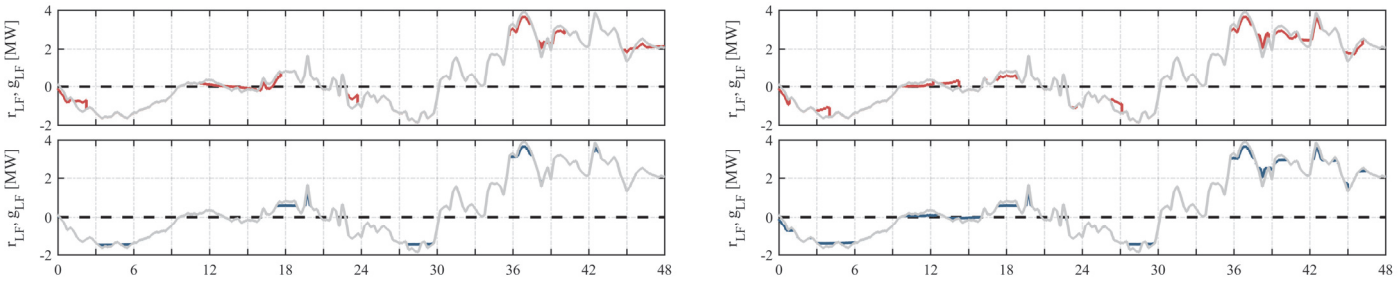

Fig. 13. The r_{LF} (gray) and g_{LF} profiles by FBM-A (top, red) and FBM-B (bottom, blue) at T = 12 h (on the left) and at T = 6 h (on the right).

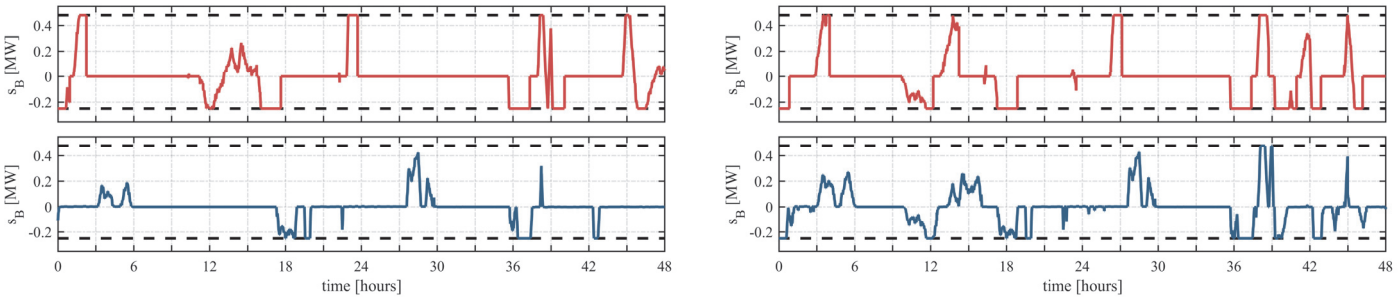

Fig. 14. B power evolutions by FBM-A (top) and FBM-B (bottom) at T = 12 h (on the left) and at T = 6 h (on the right).

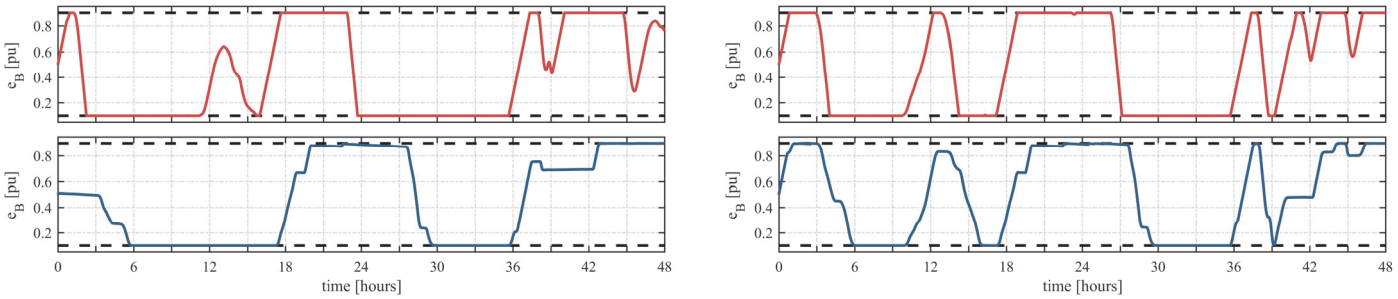

Fig. 15. B energy level by FBM-A (top) and FBM-B (bottom) at T = 12 h (on the left) and at T = 6 h (on the right).

A. Simulation Results

The overall simulation results achieved for T = 24 h are reported from Fig. 7 to Fig. 9. It can be seen that FBM-A exploits B much more than FBM-B, which, however, shows similar peak shaving capability. Particularly, FBM-A charges/discharges B as soon as the residual power profile crosses the average power threshold. Consequently, FBM-A compensates also for local power peaks, which are disregarded by the proposed FBM-B. The latter focuses on absolute power peaks only within the given time horizon, resulting in similar peak shaving capability but with a much lower B exploitation. Very good performances are achieved by both FBM-A and FBM-B in compensating for the high-frequency power fluctuations occurring on r, as pointed out by Fig. 10 through Fig. 12. Particularly, almost the same evolutions have been achieved in both cases due to the same S management. In addition, Fig. 11 reveals that S never reaches its maximum or minimum energy thresholds, it thus being able to provide this power service continuously.

Simulation results achieved for T = 12 h and T = 6 h are reported from Fig. 13 through Fig. 15. Particularly, only peak shaving capability and the corresponding B power and energy evolutions are considered because power fluctuation compensation and, thus, S operation are insensitive to the time horizon. The comparison with the previous scenario reveals that both FBM-A and FBM-B exploit B more as the time horizon decreases. However, the employment of the proposed two power thresholds enables FBM-B to detect both generation and load power peaks successfully over the given time horizon. Whereas FBM-A is unable to wait for both generation and load power peaks due to the employment of a single average power threshold. Consequently, FBM-A shows a peak shaving capability worse than FBM-B, as expected. In this context, it is worth pointing out that increased B exploitation does not always correspond to improved peak shaving capability. Particularly, the time horizon has to be chosen in accordance with the periodicity of the residual power profile, namely it should be long enough in order to enable the detection of two subsequent generation and load peaks. However, if multiple generation and/or load peaks are detected, only the greatest ones are reduced, as done by FBM-B with T = 24 h. Consequently, excessively long time horizons should be avoided as well.

In order to better highlight the peak shaving capability of both FBM-A and FBM-B, reference can be made to Fig. 16, which shows the maximum average powers achieved when the MG acts as either a generator or a load over different time windows. For example, by choosing t = 3 h, the corresponding power values represent the average powers achieved over the three hours of maximum generation and load. The results

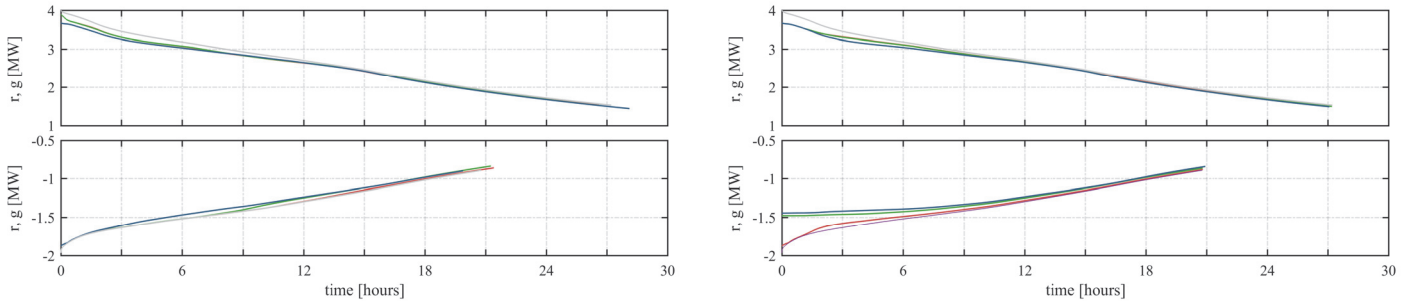

Fig. 16. Pareto diagram of averaged r (gray) and g when the MG acts as a generator and as a load achieved by FBM-A (on the left) and FBM-B (on the right) at T = 24 h (red), T = 12 h (green), and T = 6 h (blu).

TABLE IV HESS CYCLING PERFORMANCES (CYCLES OVER ONE WEEK)

	T [h]	24	12	6
FBM-A	B	9.6	9.8	12.3
	S	306.1	306.1	306.1
FBM-B	B	2.3	5.7	10.8
	S	306.1	306.1	306.1

highlight the superior performances achieved by FBM-B, especially in reducing load powers during "peak" hours.

In conclusion, the HESS performances are summed up in TABLE IV which accounts for B and S cycling performances over a week. It reveals that S cycling is totally unaffected by the variation of the time horizon in both cases, as expected. The comparison between B and S exploitation reveals the effectiveness of both FBM-A and FBM-B, which prevent B from excessive cycling due to the frequency-based power split criterion. However, B cycles achieved by FBM-B increase as the time horizon T decreases. This occurs less for FBM-A, which is characterized by a greater number of cycle and, thus, by an unsuitable B overexploitation compared to FBM-B.

V. CONCLUSION

An advanced Frequency-Based energy Management (FBM) of Hybrid Energy Storage Systems (HESSs) for Microgrids (MGs) has been presented in this paper. It consists of employing a suitable frequency-based power split criterion, together with a suitable management of B power and energy constraints based on forecasted MG residual power profile. The effectiveness of the proposed approach is verified through numerical simulations, which highlight good FBM performances, especially by employing two different power thresholds and relatively short time horizons. However, peak shaving capability could be improved further resorting to more advanced management approaches, which may also reduce the energy exchanged between the MG and the main grid. This aspect will be investigated in future works.

REFERENCES

[1] R. Hemmati and H. Saboori, "Emergence of hybrid energy storage systems in renewable energy and transport applications – A review," *Renew. Sustain. Energy Rev.*, vol. 65, pp. 11–23, Nov. 2016.

[2] L. Olatomiwa, S. Mekhilef, M. S. Ismail, and M. Moghavvemi, "Energy management strategies in hybrid renewable energy systems: A review," *Renew. Sustain. Energy Rev.*, vol. 62, pp. 821–835, Sep. 2016.

[3] L. Gao, R. A. Dougal, and S. Liu, "Power enhancement of an actively controlled battery/ultracapacitor hybrid," *IEEE Trans. Power Electron.*, vol. 20, no. 1, pp. 236–243, Jan. 2005.

[4] I. Chotia and S. Chowdhury, "Battery storage and hybrid battery supercapacitor storage systems: A comparative critical review," in *Proc. of 2015 IEEE Innovative Smart Grid Technologies - Asia (ISGT ASIA 2015)*, Bangkok (Thailand), 2015, pp. 1–6.

[5] E. Micolano, R. Lazzari, and L. Pellegrino, "Influence of management and system configuration on performances and lifetime of lithium-ion batteries," in *Proc. of AEIT International Annual Conference (AEIT 2015)*, Naples (Italy), 2015, pp. 1–6.

[6] A. Damiano, G. Gatto, I. Marongiu, M. Porru, and A. Serpi, "Real-Time Control Strategy of Energy Storage Systems for Renewable Energy Sources Exploitation," *IEEE Trans. Sustain. Energy*, vol. 5, no. 2, pp. 567–576, Apr. 2014.

[7] S. W. Alnaser and L. F. Ochoa, "Optimal Sizing and Control of Energy Storage in Wind Power-Rich Distribution Networks," *IEEE Trans. Power Syst.*, vol. 31, no. 3, pp. 2004–2013, May 2016.

[8] M. Ammar and G. Joós, "A Short-Term Energy Storage System for Voltage Quality Improvement in Distributed Wind Power," *IEEE Trans. Energy Convers.*, vol. 29, no. 4, pp. 997–1007, Dec. 2014.

[9] M. D. Mufti, S. J. Iqbal, S. A. Lone, and Q. u Ain, "Supervisory Adaptive Predictive Control Scheme for Supercapacitor Energy Storage System," *IEEE Syst. J.*, vol. 9, no. 3, pp. 1020–1030, Sep. 2015.

[10] B. Liu, F. Zhuo, Y. Zhu, and H. Yi, "System Operation and Energy Management of a Renewable Energy-Based DC Micro-Grid for High Penetration Depth Application," *IEEE Trans. Smart Grid*, vol. 6, no. 3, pp. 1147–1155, May 2015.

[11] N. Mendis, K. M. Muttaqi, and S. Perera, "Management of Battery-Supercapacitor Hybrid Energy Storage and Synchronous Condenser for Isolated Operation of PMSG Based Variable-Speed Wind Turbine Generating Systems," *IEEE Trans. Smart Grid*, vol. 5, no. 2, pp. 944–953, Mar. 2014.

[12] S. Adhikari, Z. Lei, W. Peng, and Y. Tang, "A battery/supercapacitor hybrid energy storage system for DC microgrids," in *Proc. of 8th International Power Electronics and Motion Control Conference (IPEMC-ECCE Asia 2016)*, Hefei (China), 2016, pp. 1747–1753.

[13] N. R. Tummuru, M. K. Mishra, and S. Srinivas, "Dynamic Energy Management of Renewable Grid Integrated Hybrid Energy Storage System," *IEEE Trans. Ind. Electron.*, vol. 62, no. 12, pp. 7728–7737, Dec. 2015.

[14] S. Wang *et al.*, "Design and advanced control strategies of a hybrid energy storage system for the grid integration of wind power generations," *IET Renew. Power Gener.*, vol. 9, no. 2, pp. 89–98, Feb. 2015.

[15] Y. Ye, R. Sharma, and P. Garg, "An integrated power management strategy of hybrid energy storage for renewable application," in *Proc. of 40th Annual Conference of the IEEE Industrial Electronics Society (IECON 2014)*, Dallas (USA), 2014, pp. 3088–3093.

[16] B. Hredzak, V. G. Agelidis, and M. Jang, "A Model Predictive Control System for a Hybrid Battery-Ultracapacitor Power Source," *IEEE Trans. Power Electron.*, vol. 29, no. 3, pp. 1469–1479, Mar. 2014.

[17] W. Jiang, L. Zhang, H. Zhao, H. Huang, and R. Hu, "Research on power sharing strategy of hybrid energy storage system in photovoltaic power station based on multi-objective optimisation," *IET Renew. Power Gener.*, vol. 10, no. 5, pp. 575–583, Apr. 2016.